Design of Wideband Flat Artificial Dielectric Lenses at mmWave Frequencies

Coco Martin, Caspar M.; Hu, Weiya ; Cavallo, Daniele

DOI
10.1109/TAP.2024.3357992

Publication date
2024

Document Version
Final published version

Published in
IEEE Transactions on Antennas and Propagation

Design of Wideband Flat Artificial Dielectric Lenses at mmWave Frequencies

Caspar M. Coco Martin, *Graduate Student Member, IEEE*, Weiya Hu, and Daniele Cavallo, *Senior Member, IEEE*

***Abstract*— This work aims to provide guidelines on the design of wideband flat lenses based on artificial dielectric layers (ADLs). Planar lenses based on metasurfaces are typically narrowband, due to the phase wrapping over the period of 2π that is strongly frequency-dependent. On the contrary, true-time-delay (TTD) planar lenses, which do not resort to phase discontinuities, can achieve large bandwidths. One convenient way to design wideband TTD lenses is by means of ADLs, which are stacks of subwavelength-period patch arrays embedded in a host medium to increase its effective permittivity. Tradeoffs including bandwidth, focal ratio, lens diameter, and thickness are discussed and related to the manufacturing constraints of artificial dielectrics, such as the smallest features realizable in printed circuit board (PCB) technology, which define the maximum achievable effective permittivity. An example of design is also presented, operating from 30 to 60 GHz and experimentally validated.**

***Index Terms*— Artificial dielectrics, flat lenses, ray tracing, true-time-delay (TTD) lens, wideband lenses.**

I. Introduction

DIELECTRIC lenses are commonly used quasioptical components in imaging and antenna systems. They have been used for decades in applications such as radio astronomy [1], [2], radar, and satellite communications. Lens antennas provide high-gain-radiation characteristics and can support beam scanning capability by lateral displacement of the feed. Multiple beams can also be generated simultaneously with a lens antenna system by placing multiple feeds in the focal plane. Recent advances in millimeter-wave (mmWave) and terahertz (THz) technology for high-speed wireless communication and high-resolution radars have increased the popularity of dielectric lenses for multibeam high-gain antennas [3].

Conventional homogeneous dielectric lenses have excellent properties but are typically bulky and electrically thick. Flat lenses are low profile and can be fabricated more easily compared to curved lenses, making them desirable at mmWave frequencies. Planar multibeam thin-lens antennas can be realized as Fresnel lenses [4], transmitarrays [5], or metasurfaces [6]. However, one of the limitations of these solutions is the narrow frequency bandwidth, due to the phase wrapping along the aperture, which results in sudden discontinuous jumps in the phase distribution. In some designs based on periodic structures, the band is also limited by the resonant nature of the unit cell.

To overcome the bandwidth limitations, one can employ true-time-delay (TTD) lenses that provide wideband behavior. One example is a gradient index (GRIN) lens consisting of a dielectric cylinder with a radial gradient of the refractive index. The large bandwidth is obtained at the cost of increased thickness [7]. One possibility to reduce the thickness of wideband TTD lenses is to use high-permittivity materials [8]. With such an approach, to reduce the reflection losses that would be caused by the high permittivity, matching layers must be employed to improve the transmission at the air–lens interface [9].

The varying refractive index in the lens can be artificially realized with a single material in which voids are included [10], [11], [12], [13]. By locally changing the volume fraction of air with respect to the dielectric, the desired refractive index profile can be synthesized. However, this type of artificial dielectrics is characterized by an effective permittivity equal to or lower than the one of the host medium. Thus, it is not suitable for high permittivity lens designs with reduced thickness. To realize high permittivity materials, with refractive indices that can be much larger than the ones of commercially available dielectrics, artificial dielectric layers (ADLs) can be employed [14]. These are a cascade of periodic arrays composed of subwavelength patches (capacitive gratings) to boost the effective refractive index by providing increased phase shift for a plane wave propagating within the artificial medium. TTD lens designs based on such periodic structures with subwavelength elements were presented in [15] and [16].

Recent advances in the analysis of ADLs have resulted in closed-form expressions to represent the equivalent capacitance of each layer [17], [18], [19], for general nonperiodic layer stacks. These expressions include higher-order Floquet wave interaction between layers and remain accurate even for very small interlayer distances. The availability of analytical models allows for estimating the phase shift and the scattering parameters of a unit cell with negligible computational resources.

With the aid of the closed-form modeling tools, in this work, we present an investigation of artificial dielectric flat lenses, based on a tradeoff analysis between lens performance and manufacturing complexity. The study links the maximum phase variation required for a given lens design to the parameters of the artificial dielectric. Although similar lenses as the one described in this article have been proposed in the past,

Manuscript received 30 August 2023; revised 13 November 2023; accepted 14 January 2024. Date of publication 26 January 2024; date of current version 15 February 2024. *(Corresponding author: Daniele Cavallo.)*

The authors are with the Terahertz Sensing Group, Delft University of Technology, 2628 CD Delft, The Netherlands (e-mail: c.m.cocomartin@tudelft.nl; w.hu-11@student.tudelft.nl; d.cavallo@tudelft.nl).

Color versions of one or more figures in this article are available at https://doi.org/10.1109/TAP.2024.3357992.

Digital Object Identifier 10.1109/TAP.2024.3357992

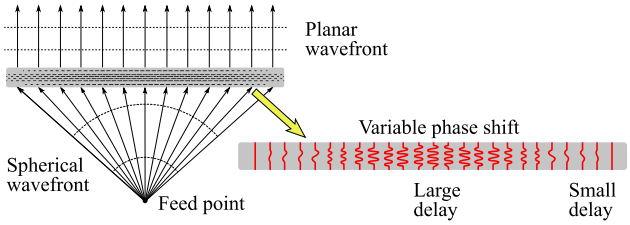

Fig. 1. Focusing flat lens, converting a spherical wavefront into a planar wavefront by a varying phase shift, implemented using subwavelength metallic inclusions.

the present study provides a systematic approach to design ADL-based flat lenses with a desired bandwidth and gain performance, while keeping a compact thickness.

We also introduce a modeling procedure for estimating the performance of the artificial dielectric lens with minimal computational load. On the contrary, simulations based on commercial software are lengthy due to the large number of electrically small metal structures to be meshed. The proposed method is based on the following steps: 1) geometrical optics to describe the feed illuminations; 2) ray tracing that includes the anisotropy of the ADLs to estimate the propagation within the lens; 3) equivalent circuit of ADL under generic plane wave incidence to find the transmitted field; and 4) physical optics to estimate the radiation pattern from the aperture field. The combination of steps 2) and 3) allows to improve the accuracy of the method with respect to the assumption of local periodicity of the ADLs. The core of the modeling part was developed as the first author's master thesis [20].

With the aid of the analysis tool, an example flat lens design is also presented, operating from 30 to 60 GHz, with a focal ratio of 0.67 and a diameter of six wavelengths at the highest frequency of operation. Based on this design, a prototype has been manufactured and tested with an open-ended waveguide feed.

The article is structured as follows: in Section II, a tradeoff analysis of flat lenses is presented, where the link between geometrical parameters, performance indicators, and manufacturing constraints is highlighted. Section III describes the steps of the modeling approach, based on a hybrid method that combines geometrical optics, physical optics, ray tracing, and analytical description of ADLs. The design steps for a specific lens are presented in Section IV, together with simulation results. In Section V, the experimental results from the prototype demonstrator are shown, to validate the design. Concluding remarks are given in Section VI.

II. Tradeoff Analysis

The flat lens under analysis generates a collimated beam by converting a spherical wavefront into a planar wavefront, as depicted in Fig. 1. The lens provides a phase shift that is larger in the center and smaller toward the lens edges, to compensate for the different path lengths of the rays emanating from the feed point and impinging at different locations on the lens. In this work, the phase shift is achieved by means of ADLs with spatially varying effective refractive indices.

A. Phase Variation

The key parameter for a TTD lens design is the maximum phase variation needed across the aperture, that is, the phase

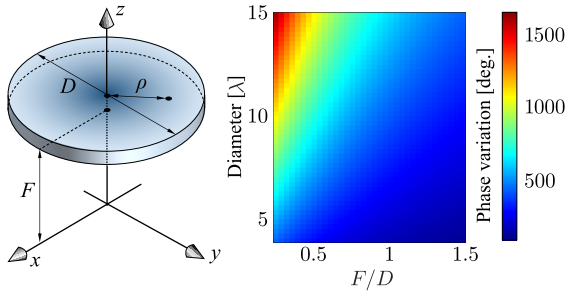

Fig. 2. (a) Geometry of the lens with diameter D and focal distance F and (b) map of maximum phase variation in degrees for different values of the diameter D and the focal ratio F/D.

difference between the center and the edge of the lens. For a lens characterized by focal length F and diameter D, the maximum phase variation depends on the lens diameter in terms of the wavelength (λ) and on the focal distance to lens diameter (F/D) ratio. For a point on the lens at distance ρ from the center, the phase variation can be expressed as $k[(F^2+\rho^2)^{0.5}-F]$, where k is the wavenumber.

For a given electrical size of the lens, the maximum phase variation increases for smaller F/D, because the smaller radius of curvature of the spherical wavefront causes larger differences in the path length of the impinging rays. Similarly, for a fixed F/D, the phase range increases as a function of the lens diameter. For designing a lens, one could generate a map of the maximum phase variation for different values of lens diameter D and focal ratio F/D, as shown in Fig. 2. These values can then be related to the design parameters of the artificial dielectric unit cell.

B. Unit Cell Concept

For the design, the lens is divided into unit cells with period p, as shown in Fig. 3, and the continuously varying refractive index is discretized. The center unit cell is assumed to be composed of a core layer with maximum effective refractive index $n_{\max}$ and two matching sections above and below to reduce reflections. All the other unit cells have a similar configuration but with a lower refractive index in the core section. The refractive index decreases gradually toward the periphery of the lens and is equal to $n_{\min}$ in the edge unit cell.

The idealized unit cell can be practically implemented by ADLs, where the geometry of the metallic patches is chosen such that the phase shift through the unit cell is equal to the desired one. The ADL can be designed using a synthesis procedure based on the closed-form equivalent layer susceptance derived in [17], [18], and [19]. This yields an equivalent circuit for both transverse electric (TE) and transverse magnetic (TM) modes for each of the unit cells forming the lens.

C. Lens Thickness

The thickness of the lens depends mainly on the maximum required phase shift, the maximum refractive index in the core, and the target frequency bandwidth over which reflection losses are below a desired level.

The schematic unit cell allows estimating the total phase shift that can be obtained for a given value of the core refractive index n_{core} and a certain total height h. Different

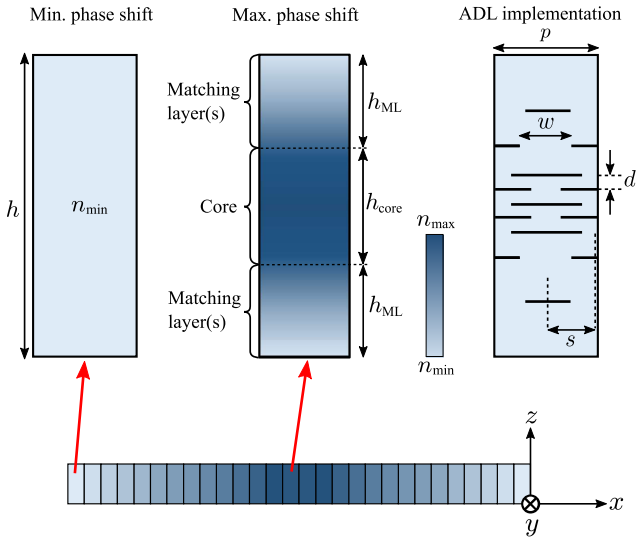

Fig. 3. Lens discretization, idealized unit cell concept, and equivalent ADL implementation.

types of matching layers can be realized, based on standard impedance transformer theory [21]. For the sake of simplicity, we assume that the matching layers are realized as an exponentially tapered impedance transformer between free space and the core material, with intrinsic impedance Z_{FS} and $Z_{\mathrm{core}} = Z_{\mathrm{FS}}/n_{\mathrm{core}}$, respectively. For example, for the lower matching layer, we can write

$$Z(z) = Z_{\mathrm{FS}} e^{az} \text{ for } 0 \le z \le h_{\mathrm{ML}} \tag{1}$$

where a is

$$a = \frac{1}{h_{\mathrm{ML}}} \ln\left(\frac{Z_{\mathrm{core}}}{Z_{\mathrm{FS}}}\right). \tag{2}$$

Writing (1) in terms of refractive index, we have

$$Z(z) = \frac{Z_{\mathrm{FS}}}{n(z)} = Z_{\mathrm{FS}} e^{az} \Rightarrow n(z) = e^{-az} \tag{3}$$

so that the phase shift of the matching layer with height h_{ML} can be found in closed form

$$\phi = k_0 \int_0^{h_{\mathrm{ML}}} n(z) dz = k_0 \int_0^{h_{\mathrm{ML}}} e^{-az} dz = \frac{k_0(1 - e^{-a h_{\mathrm{ML}}})}{a}. \tag{4}$$

The same phase shift is obtained for the top matching layer. We assume that the amplitude of the reflection coefficient for an exponential taper can be approximated as [21]

$$|\Gamma| = \frac{1}{2} \ln\left(\frac{Z_{\mathrm{core}}}{Z_{\mathrm{FS}}}\right) \mathrm{sinc}(k_0 h_{\mathrm{ML}}). \tag{5}$$

The height h_{ML} can be chosen such that the total reflection coefficient of the unit cell is better than a desired value over a target bandwidth. For example, we can choose $\Gamma \le -13$ dB over a relative frequency band $\ge$40% (from $0.66f$ to f, where f is the maximum frequency of operation), which corresponds to a total reflection $\Gamma \le -10$ dB for the two matching layers combined. These conditions define the matching section height h_{ML}. In turn, the height of the core section can be defined as $h_{\mathrm{core}} = h - 2h_{\mathrm{ML}}$. In Fig. 4, the results of this analysis are shown by plotting the maximum phase variation as a function

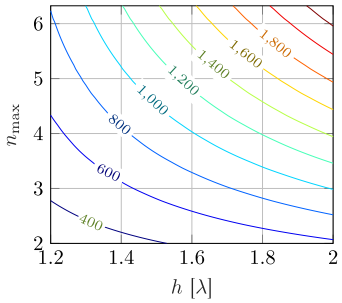

Fig. 4. Maximum phase variation as a function of the maximum effective permittivity and total lens thickness, for a flat lens with a 40% bandwidth (refection coefficient < -10 dB), assuming an exponentially tapered transformer above and below the core.

of $n_{\max}$ and h, assuming $n_{\min} = 1$ for the edge unit cell. If, for example, a certain lens design requires 800° of phase range, one can use a material with a refractive index of 6 for the core of the center unit cell and obtain a lens thickness of 1.2λ. Alternatively, if the maximum refractive index that can be achieved is 3, a lens of 1.8λ height would be required to achieve the same phase shift. It can be seen that, with the considered high values of core refractive index, several multiples of 360° can be achieved even with moderate lens thicknesses between one and two wavelengths.

D. Technology Constraints

The value of $n_{\max}$ is dependent on the manufacturing technology under consideration. The refractive index is proportional to the spatial density of the metal patches. The constraints taken into account are the following.

1) Minimum gap width between patches.
2) Dielectric host material for the patches.
3) Minimum vertical distance between patch layers, that is, the minimum thickness of dielectric spacers.
4) ADL period.

The period of the ADL has to be small compared to the wavelength at the maximum frequency. This condition is essential for keeping low current intensity on the patches and, in turn, low Ohmic losses. Moreover, the assumption of small patches is needed for the validity of the analytical descriptions of the ADL [17], [18], [19]. The analytical expressions are typically valid for ADL periods lower than a quarter wavelength.

From these constraints, a hypothetical unit cell is designed with the minimum gap width between the patches, minimum vertical spacing d, maximal lateral shifts s between the metal layers, a period $p < \lambda/4$, and using the selected dielectric as the host material. This unit cell provides the maximum effective refractive index and is used as the core in the center of the lens, to achieve the maximum possible phase shift.

III. Modeling of the Lens

In this section, we describe the steps used to analyze the lens performance. The method starts with modeling the feed in terms of its radiated pattern. We assume here that the lens is located at a far-field distance from the feed. By interpreting the far-field pattern as an angular spectrum of plane waves, one can consider a plane wave impinging locally on the lens with a certain amplitude, phase, polarization, and incident angle.

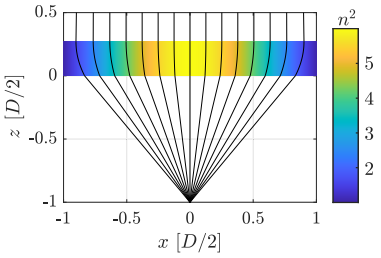

Fig. 5. Rays computed through a lens with varying refractive index, designed using the method described in [22].

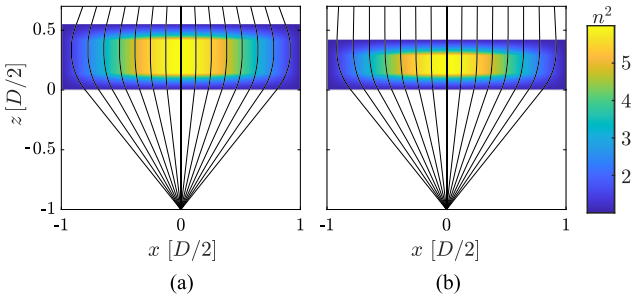

Fig. 6. Ray tracing for the same lens in Fig. 5, with exponentially tapered matching layers added (a) without compensation of the core thickness and (b) with the core thickness reduced to 55% of its original thickness.

Typically, for transmitarrays and metalenses, it is assumed that the unit cell upon which a plane wave impinges is locally periodic. This approximation is valid for gradual variations of the geometry and for thin structures. The scattering parameters of this unit cell under Floquet boundary conditions are then utilized to estimate the transmitted field by the lens. However, for large incident angles or electrically thick lenses, the incident wave can traverse multiple unit cells, reducing the accuracy of the local periodicity approximation. This problem is more evident for small F/D ratios, which result in large incident angles on the lens.

To overcome these challenges, we propose a hybrid method that combines ray tracing with the analytical description of ADLs, enabling efficient analysis of such lenses without the need for full-wave simulations.

A. Ray Tracing

To model the propagation through the lens, the Eikonal equation governing ray propagation in inhomogeneous media is solved numerically as an ordinary differential equations (ODEs) system, following the steps described in Appendix A. Given the initial conditions, that is, a starting point and a direction, the ray path in the inhomogeneous medium can be computed. The MATLAB built-in `ode45` solver is used to compute the ray paths. At any discontinuity of the refractive index distribution, Snell's law is applied. This happens at the lower and upper interfaces of the lens and at the transition between the core and the matching layers.

An example result from the ray tracing is shown in Fig. 5 for a simple GRIN lens designed following the procedure in [22]. The lens is characterized by $F/D = 0.5$, $n^2_{\max} = 6$, $n^2_{\min} = 1$, and thickness $h = 0.14\ D$. In this example, the reflection losses at the lens top and bottom interfaces are not addressed. However, especially when the GRIN lens is designed with a large maximum refractive index to reduce its thickness, the incident field from the source can undergo strong reflections at the lens-air interfaces. Thus, we also show in Fig. 6(a) the ray tracing solution for the same lens when matching layers are included. Exponential transformers are used as matching layers above and below the GRIN lens design, which is now referred to as the core. It can be noted that the inclusion of the matching layers causes an additional bending of the rays that are converging when exiting the lens, rather than parallel. This effect can be compensated by reducing the core thickness. For this example design, the lens regains its collimating function by reducing the core thickness to 55% of the original thickness, as can be seen in Fig. 6(b).

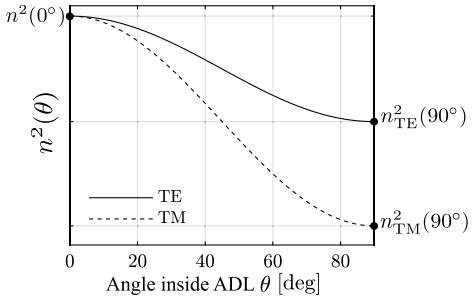

Fig. 7. Effective refractive index of a plane wave propagating through an ADL as a function of the angle inside the material.

B. Anisotropy in ADLs

The ADLs behave as an anisotropic material. Therefore, the refractive index changes as a function of the incidence angle. The squared effective refractive index in an ADL as a function of the angle of propagation θ inside the ADL follows the characteristic behavior shown in Fig. 7. This variation can be approximated with a squared cosine shape, as follows:

$$n^2_{Ti}(\theta) \approx (n^2(0°) - n^2_{Ti}(90°))\cos^2\theta + n^2_{Ti}(90°) \tag{6}$$

where n_{Ti} corresponds to either the TE or TM mode. Therefore, to fully characterize the ADL in terms of its effective refractive index for any angle θ, only the effective refractive index for normal incidence ($\theta = 0°$) and for grazing incidence ($\theta = 90°$) for TE and TM modes are required.

We can assume that the refractive index for normal incidence is known as $n_{TM}(0°) = n_{TE}(0°) = n(0°)$ as it is a design parameter. The interlayer distance d is also known, as it is determined by the selected manufacturing technology. With these assumptions, the expressions for $n^2_{TM}(90°)$ and $n^2_{TE}(90°)$ can be derived, as described in Appendix B, which gives

$$n^2_{TM}(90°) = n^2_{\mathrm{host}}\,. \tag{7}$$

$$n^2_{TE}(90°) = n^2_{\mathrm{host}} + \left(\frac{1}{k_0 d}\cos^{-1}\left(1 - \frac{\zeta k d B}{4}\right)\right)^2 \tag{8}$$

where k_0 is the free-space wavenumber, and k and ζ are the wavenumber and the impedance of the host medium with refractive index n_{host}, respectively. B is the layer susceptance, which can be expressed as

$$B = \frac{2}{\zeta}\frac{\cos(kd) - \cos(k_0 d n(0°))}{\sin(kd)}\,. \tag{9}$$

It is interesting to note that B only depends on the vertical spacing between metal layers d, the refractive index of the

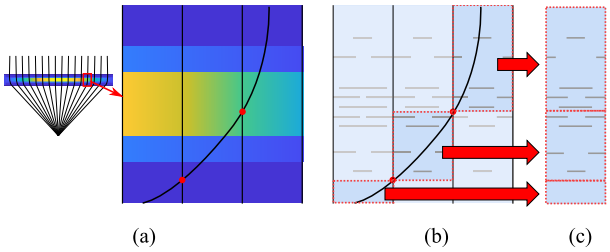

Fig. 8. Illustration of the proposed hybrid lens model. (a) Ray path is computed through a nonhomogeneous dielectric lens. (b) Ray path is overlaid on the ADL implementation of the flat lens, and the different parts of the unit cells crossed by the ray are identified (marked in red). (c) Partial unit cells are combined into a single unit cell.

host medium, and the desired value of the effective refractive index for normal incidence $n(0°)$. Since these parameters are known based on technological constraints, the values of $n_{Ti}(\theta)$ can be determined before designing the specific unit cells. By using the closed-form expression of $n_{Ti}(\theta)$ when solving numerically (14), (17), and (18), the anisotropy of the ADLs can be taken into account when computing the ray paths through the lens.

C. Combined Unit Cell

With the knowledge of the ray paths through the lens, one can compute the transmission through the lens by combining the ray propagation with the analytical ADL model presented in [19]. The method in [19] provides an equivalent circuit for the ADLs, where each layer is represented as an equivalent reactance that can be expressed in closed form. The circuit allows estimating the reflection and transmission of a generic plane wave (TE or TM, oblique incidence) through the layer stack. However, the method in [19] only applies to periodic unit cells.

On the other hand, when considering GRIN lenses, the rays can pass through different unit cells, thus the assumption of periodicity is no longer valid. To overcome this problem, we propose the approach described in Fig. 8. We first identify the regions of each unit cell that the ray traverses and then we create a new unit cell that combines these regions. Finally, we apply the equivalent model of ADLs to this combined stratification.

Since in the equivalent transmission line models the bending of the rays cannot be modeled, when computing the S-parameters, S_{12} of the transmission line model only accounts for the phase shift along z. To also account for the phase shift in the ρ direction, an adjusted $S_{12,\text{adj}}$ is defined as

$$S_{12,\text{adj}} = S_{12} e^{-jk_0 \sin(\theta_i)|\rho_t - \rho_i|} \tag{10}$$

where θ_i is the incident angle on the unit cell, and ρ_i and ρ_t are the radial distances (from the lens center) of the points at which the ray enters and exits the lens, respectively.

D. Transmitted Field and Radiation Patterns

To find the transmitted E-field after the lens $\boldsymbol{E}_t$, the θ- and ϕ-components of the incident E-field before the lens $\boldsymbol{E}_i$ are found by expressing the field radiated by the feed as a spectrum of plane waves, as shown in Fig. 9(a). Each plane wave is multiplied by the adjusted S_{12} of the combined unit cell for TM and TE modes, respectively, given by the equivalent transmission lines in Fig. 9(b). Furthermore, to satisfy the conservation of energy, the intensity law of geometric optics is applied [23], yielding

$$\boldsymbol{E}_t = \frac{A_i \cos\theta_i}{A_t \cos\theta_t} (E_{i,\theta} S_{12,TM,\text{adj}} \hat{\boldsymbol{\theta}} + E_{i,\phi} S_{12,TE,\text{adj}} \hat{\boldsymbol{\phi}}) \tag{11}$$

where θ_i and θ_t are the angle of incidence and transmit angle, respectively, found using raytracing. A_i and A_t are the ray-tube cross sections at the bottom and top of the lens.

From the E-field after the lens, Schelkunoff's formulation of the equivalence theorem is applied to find the equivalent currents, which in turn are used to compute the radiation pattern of the lens by physical optics [see Fig. 9(c)]. In Fig. 10, a comparison is given between the far-field radiation pattern computed using the proposed method and the pattern obtained with CST Microwave studio. The patterns estimated by both methods are similar, with less than 0.5 dB difference for the maximum directivity. For this particular example, the F/D is 0.25, the lens diameter is 5.5λ, and a short electric dipole is assumed as feed.

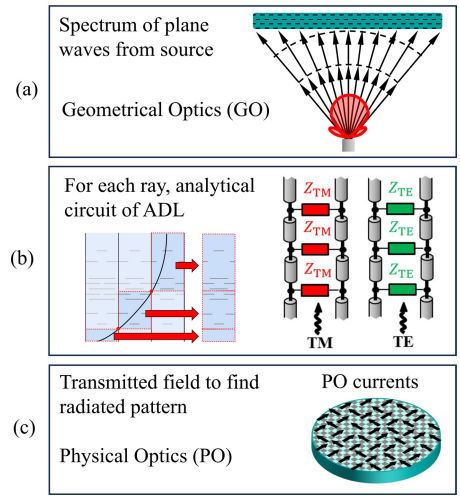

Fig. 9. Steps of the lens analysis: (a) geometrical optics to describe the field from the feed as a plane wave spectrum, (b) ray tracing and transmission line model of ADL to find the transmitted field, and (c) physical optics to compute radiation pattern.

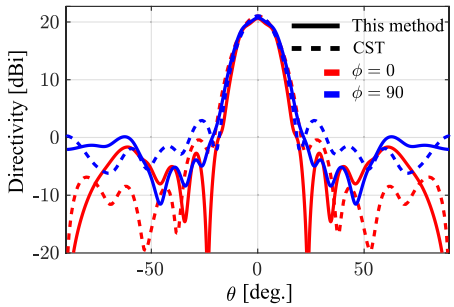

Fig. 10. Comparison between the far-field radiation patterns computed using our proposed analysis method and CST Microwave Studio.

IV. Lens Design

To verify the design procedure, a flat lens with $F/D = 0.67$ operating in the frequency band from 30 to 60 GHz is designed. The lens diameter is 30 mm, equal to 6λ at the highest frequency.

A. Technology Constraints and Maximum Refractive Index

The host material permittivity is chosen as Rogers RO4003C[1], with a relative permittivity of 3.55 and loss tangent of 0.0027 (at 10 GHz). For standard printed circuit board (PCB) processes, the minimum metal gap and track width are assumed to be 130 μm. The minimum thickness of the material is 203 μm. The period for the ADL is chosen as 1.2 mm so that the patches are smaller than a quarter wavelength within the frequency band.

Taking into account these values, the maximum effective refractive index that can be achieved is approximately 4.7. This value can be retrieved by applying (22)–(24) in Appendix B, together with the closed-form expression of the layer susceptance from [19].

B. Refractive Index Distribution

As a starting point, to find the refractive index distribution, the design formulas for GRIN lenses from [22] are used. These formulas provide a refractive index profile that varies along x but is constant in z, as in the example shown in Fig. 5. Such a lens would yield high reflections at the interface with air, especially in the central part of the lens that is electrically dense.

To avoid this problem, a two-section matching layer is added above and below the lens, which is now referred to as the core. To ensure high transmission over wide bandwidth, while easing the manufacturing, some notable design choices for the matching layers are made.

1) The absolute length of each transformer section is fixed and kept constant over the aperture. This means that not everywhere the transformer sections are $\lambda/4$ at the central frequency.
2) The outer matching layer permittivity $\varepsilon_{r,\text{outer}}$ is fixed to a constant value of 2, to be realized by means of perforations in the dielectric.
3) The inner matching layer permittivity is chosen as $\varepsilon_{r,\text{inner}} = (\varepsilon_{r,\text{outer}}\varepsilon_{r,\text{core}})^{1/2}$ and realized using ADLs.

After adding the matching layers above and below the lens, the thickness of the core h_{core} is reduced to 73% of the initial thickness, to reestablish the flat planar wavefront (as described in Fig. 6). A cross section of the lens, indicating the refractive index distribution, is shown in Fig. 11(a). To ease the manufacturing process, the minimum refractive index in the core and inner matching layer is chosen to be that of the host material.

C. ADL Implementation

The lens is divided into square unit cells with the same period of the ADL, resulting in 25 unit cells across the lens diameter. The continuous refractive index distribution is sampled in the center of each unit cell and quantized according to these values.

For each ideal unit cell, made by homogeneous slabs, a synthesis procedure is used to synthesize the equivalent ADL structure.

1) The distance between metal layers d and the host medium is fixed, based on the PCB process.

[1]Trademarked.

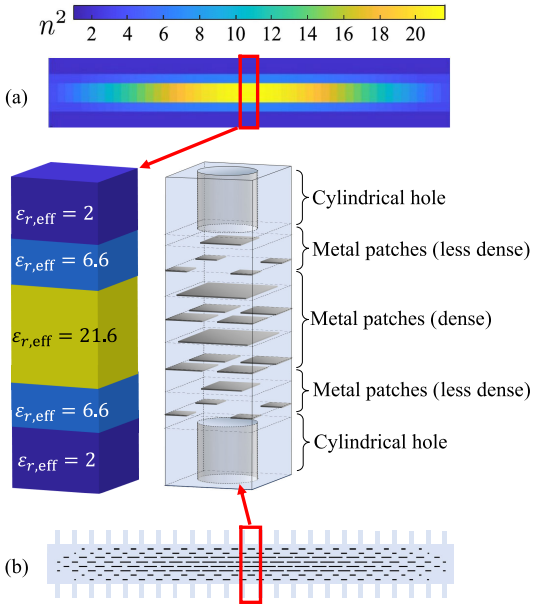

Fig. 11. Cross section of (a) refractive index distribution of the proposed lens design and (b) implementation of the lens with ADLs, with a 3-D view of the central unit cell.

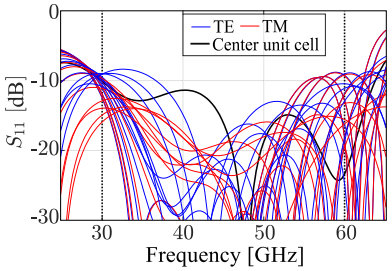

Fig. 12. S_{11} for all unit cells of the lens, for TE and TM oblique incidence.

2) The width of the gap between patches w is varied and mapped to the effective permittivity, following the procedure described in [24].
3) Each ADL slab is synthesized separately.
4) The ADL slabs are combined and the layers are tuned to match the S-parameters of the original unit cell with homogeneous slabs.

All the ADL unit cells, designed assuming local periodicity, are combined to form the entire lens, whose cross section is shown in Fig. 11(b).

The reflection coefficient of all designed unit cells is evaluated under TE and TM plane-wave illumination with the corresponding incidence angle from the feed, as shown in Fig. 12. Most curves exhibit values below -10 dB over the target bandwidth.

D. Detailed Stackup

To reduce the manufacturing costs, the lens stackup is divided into different sections, some of which have the same layer stack, so that they can be manufactured in the same PCB process: a spacer, consisting of a single layer of Rogers RO4003C laminate, separating two halves of the lens; two multi-layer PCBs with four metal layers, which include part of the core and the inner matching layer; two outer matching layers, which contain perforations. All the different sections are assembled together to form the entire lens, using plastic

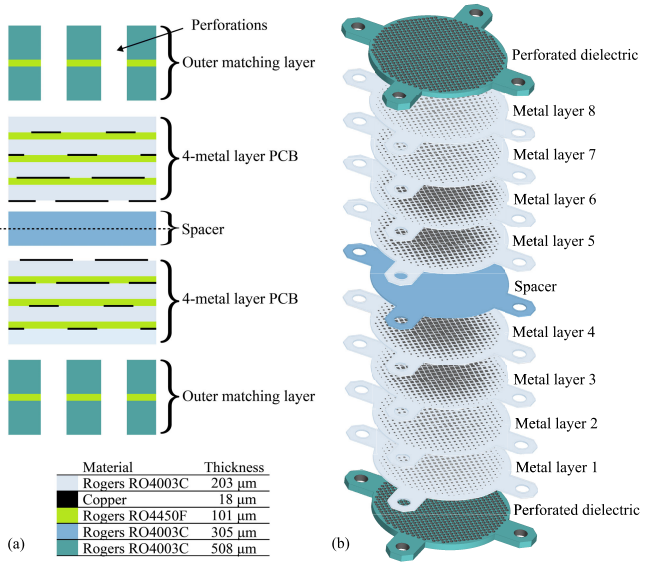

Fig. 13. (a) Exploded view of the lens layers and (b) detailed stackup with used materials. The lens is composed of two four-layer PCBs, separated by a spacer, and perforated dielectrics above and below as outer matching layers.

TABLE I
ADL DIMENSIONS [mm]

Unit cell	w_{core}	w_{ML}	Unit cell	w_{core}	w_{ML}
1	0.23	0.61	8	0.44	0.75
2	0.23	0.61	9	0.51	0.81
3	0.24	0.62	10	0.60	0.88
4	0.26	0.64	11	0.75	0.89
5	0.28	0.67	12	0.90	0.96
6	0.31	0.71	13	No metal	No metal
7	0.37	0.72			

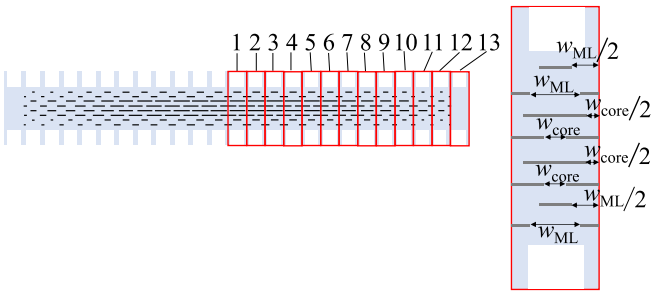

Fig. 14. Numbering of unit cells and geometrical parameters of the ADLs.

screws. The complete stackup is given in Fig. 13 and has a total thickness of 4.8 mm. The geometrical parameters of the ADLs in each unit cell are defined in Fig. 14 and their values are reported in Table I.

Since the outer matching layer should have a constant permittivity of 2 over the complete aperture, all perforations in this layer have the same size. To determine the size of the holes in the outer matching layers, a simulation of a 1×1 mm^2 unit cell is made, consisting of the host material with a circular hole of variable radius. The simulation results are plotted in Fig. 15 and show the effective permittivity as a function of the hole radius, normalized to the period. To achieve an effective permittivity of 2 at 45 GHz, perforations with a radius of 0.4 mm are selected.

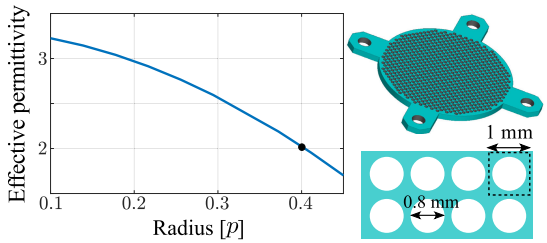

Fig. 15. Effective permittivity of 1×1 mm unit cell with a varying hole radius at 45 GHz.

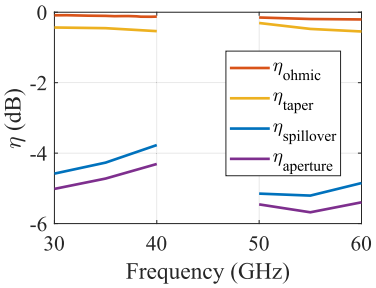

Fig. 16. Simulated efficiency of the lens with WR-28 open-ended waveguide feed in the 30–40-GHz band and WR-15 waveguide feed in the 50–60-GHz band.

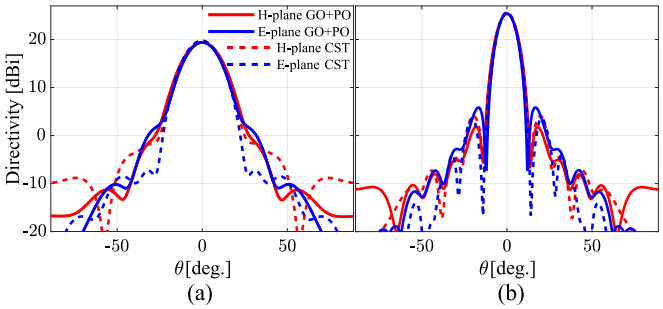

Fig. 17. Simulated far-field radiation patterns of the lens design in the E- and H-planes at (a) 30 GHz and (b) 60 GHz. Both our simulation procedure and CST are shown.

E. Simulated Patterns

To test the lens design, a simple feed is considered in this work, consisting of an open-ended waveguide. Two standard waveguides are used for different subbands: a WR-28 waveguide with cross section 7.11×3.56 mm^2, which operates in the 26.5–40-GHz band, and a WR-15 waveguide with cross section 3.76×1.88 mm^2, which operates in the 50–75-GHz band. The simulated efficiency of the lens with the open-ended waveguide feeds, split in different contributions [25], is reported in Fig. 16, for the 30–40- and 50–60-GHz bands. It can be noted that the main cause of losses is the spillover, due to the wide radiation patterns of the feed. Although the considered feed yields high spillover losses, it can still be used to demonstrate the intrinsic performance of the flat ADL lens. The design of a wideband and efficient feed suitable for the proposed lens is beyond the scope of the present study.

The radiation patterns of the lens are evaluated using both our modeling approach and CST Microwave Studio and shown in Fig. 17, at 30 and 60 GHz. The two methods estimate similar directivity patterns.

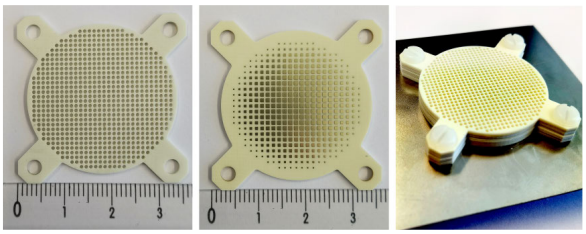

Fig. 18. Photograph of the lens prototype: (a) outer matching layer with perforations, (b) metal layer of the core, and (c) entire assembly with a metal plate.

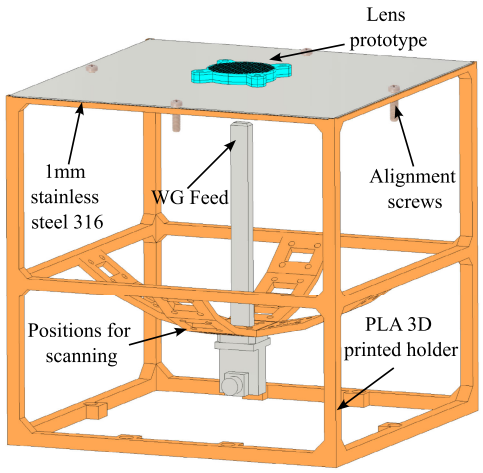

Fig. 19. Measurement setup with waveguide feed, lens, and 3-D-printed holder, made of polylactic acid (PLA) thermoplastic.

V. Experimental Validation

A prototype of the lens design was manufactured and tested. A photograph of the lens is presented in Fig. 18, which shows a top view of the perforated matching layer [Fig. 18(a)] and one of the metal layers of the core [Fig. 18(b)]. The entire assembled lens is shown in Fig. 18(c). The different sections are held together with screws at the corner and mounted on a metal plate with a circular window opening with 30-mm diameter.

The lens was measured from 30 to 40 GHz using the WR-28 open-ended waveguide as feed, and from 50 to 60 GHz using the WR-15 open-ended waveguide. For both frequency bands, a 3-D printed holder was used to position the waveguide feed and the lens, as depicted in Fig. 19. The setup also allows mounting the feed in different positions along the focal arc [26], to measure scan patterns.

A. Measured Radiation Patterns

The patterns are measured with a planar near-field scan, to which a near-field to far-field transformation is applied. The measured normalized patterns are shown in Fig. 20, compared with simulations. The co-polar (Co) component of the radiation patterns is shown in the E- and H-planes, while the cross-polar (Cx) is shown only in the diagonal plane (D-plane) since it represents the worst case. The measured patterns agree well with the simulated ones. A slightly larger discrepancy for the mainlobe beamwidth is observed at 40 GHz, which corresponds to the upper limit of operation of the WR-28 waveguide.

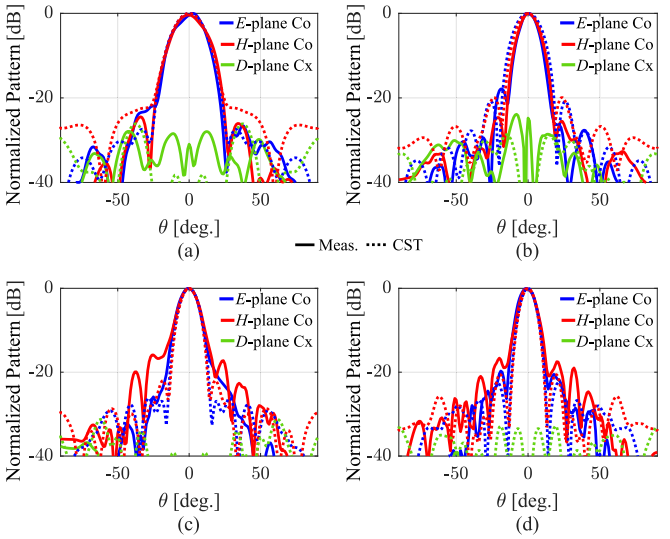

Fig. 20. Simulated and measured far-field radiation patterns at (a) 30 GHz, (b) 40 GHz, (c) 50 GHz, and (d) 60 GHz.

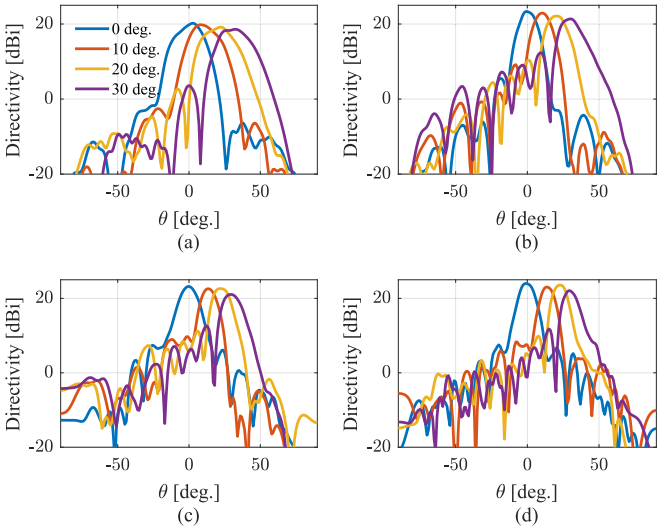

Fig. 21. Measured far-field radiation patterns for scanning in the E-plane at (a) 30 GHz, (b) 40 GHz, (c) 50 GHz, and (d) 60 GHz.

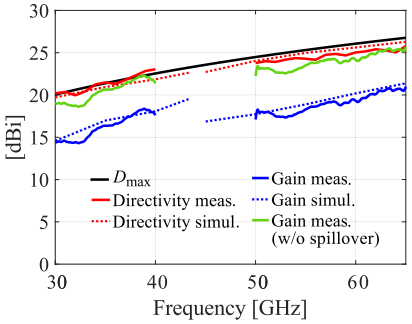

Fig. 22. Measured and simulated directivity and gain.

The directivity patterns are measured also for scanning configurations and they are presented in Fig. 21. The scan loss is close to the ideal $\cos\theta$ profile. An error of a few degrees is observed for the pointing angles with respect to the nominal directions, at the higher frequencies. This is due to a misalignment of the feed with respect to the lens due to the deformation of the plastic holder when attaching the cable on one side of the waveguide.

TABLE II
COMPARISON OF SIMILAR DESIGNS FOUND IN THE LITERATURE

Ref.	Max gain	Frequency range [GHz]	D	Thickness	Aperture efficiency	F/D
[9]	34 dBi	14-40	27λ	4λ	>31%	0.625
[22]	23.6 dBi	12-40	16λ	1.74λ	>40%*	1.25
[27]	16.3 dBi	9-11	3.6λ	0.52λ	>46%	0.3
[28]	22 dBi	8.2-12.4	4.5λ	0.33λ	>50%	0.57
[29]	18.9 dBi	60-77	6.4λ	1.8λ	>19%*	0.25
[30]	20.7 dBi	75-95	6.3λ	4.9λ	>45%	0.55
[31]	21 dBi	8-10	6.7λ	0.87λ	>24%	0.2
This work	19 dBi	30-60	6λ	0.95λ	>32%	0.67

*calculated from reported results
λ is free-space wavelength at the highest frequency

The measured broadside gain and directivity versus frequency are reported in Fig. 22 and compared with simulations. The maximum theoretical directivity from the lens aperture $D_{\max} = (\pi D/\lambda)^2$ is also reported for comparison. The largest contribution to the losses is the spillover, as expected from the use of open-ended waveguides as feeds. To emphasize this aspect, the gain compensated for the spillover (estimated from simulations) is also included in the figure. This gain is about 1 dB lower than the measured directivity across the frequency band, confirming the low Ohmic and reflection losses of the design.

The achieved results are compared with similar existing flat lens designs in Table II. Our design gives a good compromise in terms of bandwidth and compact thickness. Regarding the aperture efficiency, the minimum value of 32% is mainly determined by the use of open-ended waveguide feeds. Simulations performed with more realistic feeds (circular horn and 3×3 wideband slot array) gave an estimation of aperture efficiency greater than 55% and 60%, respectively.

VI. CONCLUSION

We presented a procedure to design wideband flat lenses based on ADLs. General considerations were given that relate different geometrical and performance parameters, including the lens diameter and F/D ratio, the lens thickness, reflection losses, bandwidth, and maximum realizable refractive index.

The lens was modeled by combining a ray-tracing method with the equivalent circuit of ADLs. A closed-form expression for the refractive index of ADLs as a function of the angle of propagation was derived and allows to account for the anisotropy of ADLs in the ray tracing. Finally, the geometrical optics/physical optics method was used to find the radiation patterns.

To verify the design procedure, a wideband (30–60 GHz) collimating lens based on ADLs was designed, with a diameter of 6λ at the highest frequency and F/D equal to 0.67. A prototype based on this design was realized in PCB technology and tested. Measured results confirmed the expected performance.

The ADL flat lenses are a good compromise between bandwidth and thickness, allowing for wide bandwidth behavior, while reducing the overall profile of the lens. These characteristics are beneficial for manufacturing and integration at mmWave and THz frequencies.

It has to be pointed out that the proposed approach yields wideband and electrically thin lens designs, but it is suitable for moderate gain/directivity levels. Larger directivities can be achieved at the cost of increased manufacturing complexity (large number of metal layers) or reduced bandwidth by resorting to Fresnel zones (phase wrapping).

APPENDIX A
DERIVATION OF THE ODE SYSTEM FROM EIKONAL EQUATION

In [32], from the Eikonal equation, the differential equation of light rays is derived and can be expressed as

$$n\frac{d\boldsymbol{r}(s)}{ds} = \nabla S \tag{12}$$

where n is the refractive index and $S(\boldsymbol{r}) =$ constant represents geometrical wavefronts. The light rays $\boldsymbol{r}(s)$ are defined as orthogonal trajectories to the wavefronts, while s indicates a position along the ray path. One can derive an ODEs system to solve for the ray trajectory, using steps similar to [33]. Writing (12) in terms of its different components explicitly leads to

$$n\frac{dx}{ds}\hat{\boldsymbol{x}} + n\frac{dy}{ds}\hat{\boldsymbol{y}} + n\frac{dz}{ds}\hat{\boldsymbol{z}} = \frac{\partial S}{\partial x}\hat{\boldsymbol{x}} + \frac{\partial S}{\partial y}\hat{\boldsymbol{y}} + \frac{\partial S}{\partial z}\hat{\boldsymbol{z}} \tag{13}$$

and defining $p_x = \partial S/\partial x$, $p_y = \partial S/\partial y$, and $p_z = \partial S/\partial z$ yields three scalar equations

$$n\frac{dx}{ds} = p_x \tag{14a}$$
$$n\frac{dy}{ds} = p_y \tag{14b}$$
$$n\frac{dz}{ds} = p_z\,. \tag{14c}$$

Differentiating (12) with respect to s yields the differential equation of the light rays

$$\frac{d}{ds}\left(n\frac{d\boldsymbol{r}(s)}{ds}\right) = \nabla n\,. \tag{15}$$

Similarly, one can explicitly write the different Cartesian components as follows:

$$\frac{d}{ds}\left(n\frac{dx}{ds}\right)\hat{\boldsymbol{x}} + \frac{d}{ds}\left(n\frac{dy}{ds}\right)\hat{\boldsymbol{y}} + \frac{d}{ds}\left(n\frac{dz}{ds}\right)\hat{\boldsymbol{z}} = \left(\frac{\partial n}{\partial x}\hat{\boldsymbol{x}} + \frac{\partial n}{\partial y}\hat{\boldsymbol{y}} + \frac{\partial n}{\partial z}\hat{\boldsymbol{z}}\right). \tag{16}$$

Substituting (14) into (16), three scalar equations can be written

$$\frac{dp_x}{ds} = \frac{\partial n}{\partial x} \tag{17a}$$
$$\frac{dp_y}{ds} = \frac{\partial n}{\partial y} \tag{17b}$$
$$\frac{dp_z}{ds} = \frac{\partial n}{\partial z}\,. \tag{17c}$$

The combination of (14) and (17) yields the full ODE system, which can be solved with existing numerical solvers, such as MATLAB `ode45`, with the initial values given by

$$x = x_0 \tag{18a}$$
$$y = y_0 \tag{18b}$$
$$z = z_0 \tag{18c}$$
$$p_x = n(x_0, y_0, z_0)\sin\theta\cos\phi \tag{18d}$$

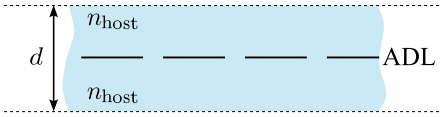

Fig. 23. Schematic of the periodic structure under investigation.

$$p_y = n(x_0, y_0, z_0)\sin\theta\sin\phi \tag{18e}$$
$$p_z = n(x_0, y_0, z_0)\cos\phi\,. \tag{18f}$$

The angles θ and ϕ define the direction of the ray in the point (x_0, y_0, z_0) where it enters the lens.

APPENDIX B
CLOSED-FORM EXPRESSIONS FOR EFFECTIVE REFRACTIVE INDEX IN ADLS

Let us consider an ADL structure composed of an infinite periodic cascade of metal layers, spaced by d. The periodic stratification is shown in Fig. 23 and it consists of an array of metal patches with dielectric spacers above and below. The dielectric slabs are assumed to be characterized by refractive index n_{host}, wavenumber k, and intrinsic impedance ζ.

One can approximate the effective refractive index of such a structure by equating the ABCD matrix of the structure in Fig. 23 to the ABCD matrix of a homogeneous equivalent material. This procedure results in the following expression of the z-component of the effective wavenumber for TE and TM waves traveling with an angle θ inside the ADL [24]:

$$k_{z,\text{eff},Ti}(\theta) = \frac{1}{d}\cos^{-1}\left(\cos(k_z d) + j\frac{Z_{Ti}}{2Z_{\text{ADL},Ti}}\sin(k_z d)\right) \tag{19}$$

where $k_z = k\cos\theta$ is the z-component of the propagation constant in the host medium, "Z_{Ti}" can refer to either TM or TE wave impedance, given by $Z_{\text{TM}} = \zeta k_z/k$ and $Z_{\text{TE}} = \zeta k/k_z$.

The layer impedances $Z_{\text{ADL,Ti}}$ are given by [24]

$$Z_{\text{ADL,TE}} = -\frac{j}{B\left(1-\frac{\sin^2\theta}{2}\right)} \tag{20}$$
$$Z_{\text{ADL,TM}} = -\frac{j}{B} \tag{21}$$

where B is the susceptance of the layer, which is typically found from the geometrical parameters of the patch array [17]. Substituting (20) and (21) in (19), we can write the explicit expression of the TE and TM effective propagation constants along z

$$k_{z,\text{eff,TE}}(\theta) = \frac{1}{d}\cos^{-1}\left(\cos(k_z d) - \frac{\zeta k B(1-\frac{1}{2}\sin^2\theta)}{2k_z}\sin(k_z d)\right) \tag{22}$$

$$k_{z,\text{eff,TM}}(\theta) = \frac{1}{d}\cos^{-1}\left(\cos(k_z d) - \frac{\zeta k_z B}{2k}\sin(k_z d)\right). \tag{23}$$

From (22) and (23), one can find the squared effective refractive index as [24]

$$n_{Ti}^2(\theta) = \frac{k_{z,\text{eff},Ti}^2(\theta) + k^2\sin^2\theta}{k_0^2}. \tag{24}$$

For TM waves incident at $\theta = 90°$, $k_z = 0$ and thus $k_{z,\text{eff,TM}} = 0$ from (23). Consequently, from (24), one can write

$$n_{\text{TM}}^2(90°) = \frac{k^2}{k_0^2} = n_{\text{host}}^2. \tag{25}$$

This result is intuitive since a TM wave incidence from $\theta = 90°$ has the electric field orthogonal to the patches and thus interacts only with the host medium.

For TE wave incidence, the expression for $n_{\text{TE}}^2(90°)$ is more complicated since the electric field is parallel to the patches and is still affected by the metal. To find an expression of $n_{\text{TE}}^2(90°)$, we first assume normal incidence, that is, $\theta = 0°$, $k_z = k$. Under this assumption, (22) becomes

$$k_{z,\text{eff,TE}}(0°) = \frac{1}{d}\cos^{-1}\left(\cos(kd) - \frac{\zeta B}{2}\sin(kd)\right). \tag{26}$$

Substituting (26) in (24) for $\theta = 0°$ gives

$$n_{TE}(0°) = \frac{1}{k_0 d}\cos^{-1}\left(\cos(kd) - \frac{\zeta B}{2}\sin(kd)\right). \tag{27}$$

Solving for B results in

$$B = \frac{2}{\zeta}\frac{\cos(kd) - \cos(k_0 d n_{TE}(0°))}{\sin(kd)}. \tag{28}$$

Once the expression for B is known, we can now evaluate (22) and (24) for $\theta = 90°$, which gives

$$n_{TE}^2(90°) = n_{\text{host}}^2 + \left(\frac{1}{k_0 d}\cos^{-1}\left(1 - \frac{\zeta k d B}{4}\right)\right)^2 \tag{29}$$

where $\lim_{k_z\to 0}[\sin(k_z d)/k_z] = 1$ is used.

ACKNOWLEDGMENT

The authors would like to thank Juan Bueno for his support in the antenna testing.

REFERENCES

[1] C. A. Fernandes, E. B. Lima, and J. R. Costa, "Broadband integrated lens for illuminating reflector antenna with constant aperture efficiency," *IEEE Trans. Antennas Propag.*, vol. 58, no. 12, pp. 3805–3813, Dec. 2010.

[2] O. Yurduseven, D. Cavallo, and A. Neto, "Wideband dielectric lens antenna with stable radiation patterns fed by coherent array of connected leaky slots," *IEEE Trans. Antennas Propag.*, vol. 62, no. 4, pp. 1895–1902, Apr. 2014.

[3] W. Hong et al., "Multibeam antenna technologies for 5G wireless communications," *IEEE Trans. Antennas Propag.*, vol. 65, no. 12, pp. 6231–6249, Dec. 2017.

[4] A. Jouade, M. Himdi, and O. Lafond, "Fresnel lens at millimeter-wave: Enhancement of efficiency and radiation frequency bandwidth," *IEEE Trans. Antennas Propag.*, vol. 65, no. 11, pp. 5776–5786, Nov. 2017.

[5] G. Liu, M. R. Dehghani Kodnoeih, K. T. Pham, E. M. Cruz, D. González-Ovejero, and R. Sauleau, "A millimeter-wave multibeam transparent transmitarray antenna at Ka-band," *IEEE Antennas Wireless Propag. Lett.*, vol. 18, pp. 631–635, 2019.

[6] M. Jiang, Z. N. Chen, Y. Zhang, W. Hong, and X. Xuan, "Metamaterial-based thin planar lens antenna for spatial beamforming and multibeam massive MIMO," *IEEE Trans. Antennas Propag.*, vol. 65, no. 2, pp. 464–472, Feb. 2017.

[7] A. Paraskevopoulos, F. Maggiorelli, M. Albani, and S. Maci, "Radial GRIN lenses based on the solution of a regularized ray congruence equation," *IEEE Trans. Antennas Propag.*, vol. 70, no. 2, pp. 888–899, Feb. 2022.

[8] F. Maggiorelli, A. Paraskevopoulos, J. C. Vardaxoglou, M. Albani, and S. Maci, "Profile inversion and closed form formulation of compact GRIN lenses," *IEEE Open J. Antennas Propag.*, vol. 2, pp. 315–325, 2021.

[9] N. C. Garcia and J. D. Chisum, "High-efficiency, wideband GRIN lenses with intrinsically matched unit cells," *IEEE Trans. Antennas Propag.*, vol. 68, no. 8, pp. 5965–5977, Aug. 2020.
[10] H. Ward, W. Puro, and D. Bowie, "Artificial dielectrics utilizing cylindrical and spherical voids," *Proc. IRE*, vol. 44, no. 2, pp. 171–174, Feb. 1956.
[11] R. Corkum, "Isotropic artificial dielectric," *Proc. IRE*, vol. 40, no. 5, pp. 574–587, May 1952.
[12] A. Petosa, A. Ittipiboon, and S. Thirakoune, "Investigation on arrays of perforated dielectric Fresnel lenses," *IEE Proc.-Microw., Antennas Propag.*, vol. 153, no. 3, pp. 270–276, 2006.
[13] J. Pourahmadazar and T. A. Denidni, "Towards millimeter-wavelength: Transmission-mode fresnel-zone plate lens antennas using plastic material porosity control in homogeneous medium," *Sci. Rep.*, vol. 8, no. 1, pp. 1–14, Mar. 2018.
[14] S. Jones and J. Brown, "Metallic delay lenses," *Nature*, vol. 163, no. 4139, pp. 324–325, Feb. 1949.
[15] M. Li and N. Behdad, "Wideband true-time-delay microwave lenses based on metallo-dielectric and all-dielectric lowpass frequency selective surfaces," *IEEE Trans. Antennas Propag.*, vol. 61, no. 8, pp. 4109–4119, Aug. 2013.
[16] C. M. Coco Martin and D. Cavallo, "Analysis and design of wideband artificial dielectric flat lenses," in *Proc. Eur. Conf. Antennas Propag.*, Florence, Italy, Mar. 2023, pp. 1–5.
[17] D. Cavallo and C. Felita, "Analytical formulas for artificial dielectrics with nonaligned layers," *IEEE Trans. Antennas Propag.*, vol. 65, no. 10, pp. 5303–5311, Oct. 2017.
[18] D. Cavallo, "Dissipation losses in artificial dielectric layers," *IEEE Trans. Antennas Propag.*, vol. 66, no. 12, pp. 7460–7465, Dec. 2018.
[19] D. Cavallo and R. M. van Schelven, "Closed-form analysis of artificial dielectric layers with non-periodic characteristics," in *Proc. 13th Eur. Conf. Antennas Propag. (EuCAP)*, Krakow, Poland, Mar. 2019, pp. 1–5.
[20] C. M. Coco Martin, "Wideband flat lenses based on artificial dielectric layers," M.S. thesis, EEMCS Faculty, Delft Univ. Technol., Delft, The Netherlands, 2022.
[21] D. M. Pozar, *Microwave Engineering*, 4th ed. Hoboken, NJ, USA: Wiley, 2012.
[22] S. Zhang, R. K. Arya, W. G. Whittow, D. Cadman, R. Mittra, and J. C. Vardaxoglou, "Ultra-wideband flat metamaterial GRIN lenses assisted with additive manufacturing technique," *IEEE Trans. Antennas Propag.*, vol. 69, no. 7, pp. 3788–3799, Jul. 2021.
[23] F. Maggiorelli, A. Paraskevopoulos, R. Giusto, M. Albani, and S. Maci, "Ray-tracing in dielectric inhomogeneous metalenses," in *Proc. 15th Eur. Conf. Antennas Propag. (EuCAP)*, Dusseldorf, Germany, Mar. 2021, pp. 1–5.
[24] W. H. Syed, "On the control of surface waves in integrated antennas," Ph.D. dissertation, Microelectronics Dept., Delft Univ. Tech., Delft, The Netherlands, 2015.
[25] P.-S. Kildal, "Factorization of the feed efficiency of paraboloids and Cassegrain antennas," *IEEE Trans. Antennas Propag.*, vol. AP-33, no. 8, pp. 903–908, Aug. 1985.
[26] J. Ruze, "Lateral-feed displacement in a paraboloid," *IEEE Trans. Antennas Propag.*, vol. AP-13, no. 5, pp. 660–665, Sep. 1965.
[27] Y. Su and Z. N. Chen, "A flat dual-polarized transformation-optics beamscanning Luneburg lens antenna using PCB-stacked gradient index metamaterials," *IEEE Trans. Antennas Propag.*, vol. 66, no. 10, pp. 5088–5097, Oct. 2018.
[28] Q.-W. Lin and H. Wong, "A low-profile and wideband lens antenna based on high-refractive-index metasurface," *IEEE Trans. Antennas Propag.*, vol. 66, no. 11, pp. 5764–5772, Nov. 2018.
[29] M. Imbert, A. Papió, F. De Flaviis, L. Jofre, and J. Romeu, "Design and performance evaluation of a dielectric flat lens antenna for millimeter-wave applications," *IEEE Antennas Wireless Propag. Lett.*, vol. 14, pp. 342–345, 2015.
[30] J. Melendro-Jimenez, P. Sanchez-Olivares, A. Tamayo-Dominguez, X. Sun, and J. M. Fernandez-Gonzalez, "3D printed directive beam-steering antenna based on gradient index flat lens with an integrated polarizer for dual circular polarization at W-band," *IEEE Trans. Antennas Propag.*, vol. 71, no. 1, pp. 1059–1064, Jan. 2023.
[31] S. M. A. M. H. Abadi and N. Behdad, "Design of wideband, FSS-based MultiBeam antennas using the effective medium approach," *IEEE Trans. Antennas Propag.*, vol. 62, no. 11, pp. 5557–5564, Nov. 2014.
[32] M. Born and E. Wolf, *Principles of Optics*, 6th ed. Oxford, U.K.: Pergamon, 1980.
[33] D. Kulyabov, M. Gevorkyan, and A. Korolkova, "Software implementation of the Eikonal equation," *Proc. Int. Conf. ITTMM*, Moscow, Russia, Apr. 2018, pp. 25–35.

Caspar M. Coco Martin (Graduate Student Member, IEEE) received the M.Sc. degree (cum laude) in electrical engineering from the Delft University of Technology (TU Delft), Delft, The Netherlands, in 2022. He is currently pursuing the Ph.D. degree with the Terahertz Sensing Group, TU Delft.

His current research interests include wideband antenna arrays, artificial dielectrics, and analytical methods for electromagnetics.

Mr. Coco Martin was a recipient of the Excellent Presentation Award at the IEEE Ukrainian Microwave Conference in 2022.

Weiya Hu received the B.Sc. degree in electric and electronics engineering from the University of Electronics Science and Technology of China (UESTC), Chengdu, China, in 2017, and the M.Sc. degree (cum laude) in electrical engineering from the Delft University of Technology (TU Delft), Delft, The Netherlands, in 2023.

For his master thesis project, carried out with the Terahertz Sensing Group, TU Delft, he worked on the design and measurements of artificial dielectric flat lenses.

Daniele Cavallo (Senior Member, IEEE) received the M.Sc. degree (summa cum laude) in telecommunication engineering from the University of Sannio, Benevento, Italy, in 2007, and the Ph.D. degree (cum laude) in electromagnetics from the Eindhoven University of Technology, Eindhoven, The Netherlands, in 2011.

From 2007 to 2011, he was with the Antenna Group, Netherlands Organization for Applied Scientific Research, The Hague, The Netherlands. From 2012 to 2015, he was a Post-Doctoral Researcher with the Microelectronics Department, Delft University of Technology (TU Delft), Delft, The Netherlands. In 2015, he joined Chalmers University of Technology, Gothenburg, Sweden, as a Visiting Researcher. He is currently an Associate Professor with the Terahertz Sensing Group, TU Delft. He has authored or coauthored more than 180 papers published in peer-reviewed international journals and conference proceedings. His current research interests include analytical and numerical methods for antenna characterization, the design of antenna arrays, and on-chip antennas.

Dr. Cavallo is a member of the European Association on Antennas and Propagation (EurAAP), the co-coordinator of the EurAAP working group "Active Array Antennas," and a Management Committee Member of the COST Action "Future communications with higher-symmetric engineered artificial materials (SyMat)." He was a recipient of the Best Innovative Paper Prize at the European Space Agency Antenna Workshop in 2008, the Best Paper Award in Electromagnetics and Antenna Theory at the 11th European Conference on Antennas and Propagation (EuCAP) in 2017, and the 250 keuro "Veni" Personal Grant from the Netherlands Organization for Scientific Research in 2015. His students received the Best Student Paper Award at EuCAP 2013, the Special Mention at EuCAP 2015, the Else Kooi Prize in 2016, and the Honorable Mention at the IEEE Antennas and Propagation Society International Symposium in 2019. He has served as an Associate Editor for IEEE TRANSACTIONS ON ANTENNAS AND PROPAGATION from 2016 to 2022.